

Gaussian-Forest: Hierarchical-Hybrid 3D Gaussian Splatting for Compressed Scene Modeling

Fengyi Zhang¹, Tianjun Zhang¹, Lin Zhang¹, Helen Huang², Yadan Luo²

¹Tongji University

²University of Queensland

{zzfff, 1911036, cslinzhang}@tongji.edu.cn, {y.luo, helen.huang}@uq.edu.au,

Abstract

The field of novel-view synthesis has recently witnessed the emergence of 3D Gaussian Splatting, which represents scenes in a point-based manner and renders through rasterization. This methodology, in contrast to Radiance Fields that rely on ray tracing, demonstrates superior rendering quality and speed. However, the explicit and unstructured nature of 3D Gaussians poses a significant storage challenge, impeding its broader application. To address this challenge, we introduce the Gaussian-Forest modeling framework, which hierarchically represents a scene as a forest of hybrid 3D Gaussians. Each hybrid Gaussian retains its unique explicit attributes while sharing implicit ones with its sibling Gaussians, thus optimizing parameterization with significantly fewer variables. Moreover, adaptive growth and pruning strategies are designed, ensuring detailed representation in complex regions and a notable reduction in the number of required Gaussians. Extensive experiments demonstrate that Gaussian-Forest not only maintains comparable speed and quality but also achieves a compression rate surpassing 10 times, marking a significant advancement in efficient scene modeling. Codes are available at <https://github.com/Xian-Bei/GaussianForest>.

1 Introduction

Over the past few years, there has been rapid development in the field of 3D vision, marked by the emergence of the Radiance Field technique designed for 3D scene representation and novel view synthesis. This development has not only established a solid foundation but also acted as a significant catalyst for further advancements. As a pioneering effort, NeRF [Mildenhall *et al.*, 2020] represents 3D scenes implicitly using Multi-Layer Perceptrons (MLPs) and employs ray tracing for rendering, resulting in high visual quality. However, this approach comes with the drawback of unacceptably slow speeds for both training and inference. Subsequent research endeavors have explored various explicit or hybrid scene representations [Liu *et al.*, 2020; Sun *et al.*, 2022] to enhance computational efficiency. Nonetheless, as these methods con-

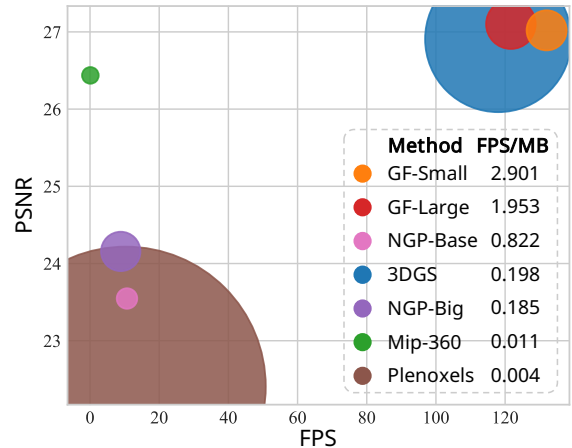


Figure 1: Quantitative comparison across 13 real-world scenes from three datasets on rendering quality, model size, and rendering speed. The size of each point in the figure indicates the corresponding model size (in MB). Our Gaussian-Forest (GF) excels in adeptly balancing rendering speed and model size. Across all scenarios, GF achieves the highest speed-to-size ratio, surpassing all baselines by a large margin while ensuring high-fidelity rendering quality.

tinue relying on ray tracing, which necessitates dense sampling across thousands of rays even in empty spaces, they encounter challenges in achieving real-time rendering rates. This challenge becomes more prominent when facing practical requirements such as high resolution, large-scale scenes, and consumer-grade devices.

As a recent revolutionary development, 3D Gaussian Splatting (3DGS) has introduced an explicitly point-based approach for scene representation, pivoting from ray tracing to rasterization for both training and rendering processes. This innovative shift has resulted in state-of-the-art visual quality and comparable training efficiency while significantly boosting rendering speed. However, it comes with a primary constraint, which lies in its substantial storage requirements. Typically, it necessitates millions of Gaussians to represent a scene, resulting in a huge model size that even reaches thousands of megabytes. Such resource-intensive demands pose a significant obstacle to its practical application, particularly in scenarios with limited resources and bandwidth.

In response to this practical challenge, we propose Gaussian-Forest for compressed 3D scene representation,

which models each Gaussian with significantly fewer parameters by organizing hybrid Gaussians in a hierarchical forest structure, while concurrently controlling their overall number via adaptive growth and pruning. Our approach is motivated by the substantial parameter redundancy observed among the millions of Gaussians employed in 3DGS [Kerbl *et al.*, 2023], where groups of Gaussians exhibit implicit associations and share similar attributes. As demonstrated in Fig. 1, Gaussian-Forest adeptly balances storage, speed, and quality. The success of Gaussian-Forest hinges on three pivotal elements.

Firstly, we introduce a hybrid representation of 3D Gaussians, termed hybrid Gaussian, which encompasses much fewer free parameters compared to the standard form by exploiting parameter redundancy. Each Gaussian maintains unique explicit attributes, such as position and opacity, while sharing implicit attributes, including the covariance matrix and view-dependent color, within a latent feature space.

Secondly, we organize hybrid Gaussians in a hierarchical manner, conceptualizing them as a forest for scene modeling. Explicit and implicit attributes of hybrid Gaussians are designated as leaf and non-leaf nodes, respectively, and interconnected through efficient pointers. In this formulation, through recursive tracing pointers upwards, each leaf node follows a unique path leading to the root of its corresponding tree, and all nodes along this path uniquely characterize a hybrid Gaussian. In addition, implicit attribute nodes at higher levels are significantly fewer in number (the quantity of root nodes is around 2% of the leaves) and are reused by a larger set of hybrid Gaussians, leading to a more compact scene representation while preserving adaptability and expressive capability.

Thirdly, we propose an adaptive growth and pruning strategy for Gaussian-Forest. This dynamic growth relies on cumulative gradients to discern regions characterized by under-reconstruction or high uncertainty, such as object boundaries or regions with notable view-dependency. The expansion of new nodes in these complex regions facilitates swift scene adaptation, even with sparse or imprecise initial points. Simultaneously, regularly identifying and pruning insignificant leaves and branches, such as trivial Gaussians in simple regions like backgrounds, provides effective control over the total number of nodes. This ensures concise representations without compromising rendering quality, while contributing to the acceleration of both training and rendering. The primary contributions of this paper are summarized as follows:

- Introducing Gaussian-Forest, which represents a scene as a forest composed of hybrid Gaussians. By modeling each Gaussian with significantly fewer parameters, remarkable compactness is achieved while adaptability and expressiveness are retained.
- Developing adaptive growth and pruning strategies specifically tailored for Gaussian-Forest, facilitating rapid scene adaptation while avoiding unnecessary expansion of the number of Gaussians.
- Extensive experiments showcase Gaussian-Forest’s consistent attainment of comparable rendering quality and speed with a compression rate exceeding $10\times$, strongly affirming its efficacy as an efficient technique for scene representation.

2 Related Work

Neural Radiance Field (NeRF) was introduced as a milestone for scene representation and novel view synthesis by [Mildenhall *et al.*, 2020]. Subsequent work has since amplified this concept, with notable strides made across various fronts, such as regularization [Kim *et al.*, 2022; Niemeyer *et al.*, 2022], supervision [Wei *et al.*, 2021; Deng *et al.*, 2022; Yu *et al.*, 2022], and extended applications like dynamics [Pumarola *et al.*, 2021; Cao and Johnson, 2023] and editing [Yuan *et al.*, 2022; Zhou *et al.*, 2023]. Among these, the evolution in the scene representation and rendering paradigms stand as particularly profound advancements.

Implicit and Explicit Scene Representation

NeRF [Mildenhall *et al.*, 2020] employs MLPs with compact size and continuous representation to model scenes. However, neural implicit representation leads to notably low time efficiency, attributed in part to long inference times of deep MLPs. Adhering to the principle of trading space for time, Plenoxels [Wei *et al.*, 2021] partitions the 3D space and stores associated attributes within each grid. However, high-resolution grids are necessary for detailed rendering, significantly escalating storage requirements. TensoRF [Chen *et al.*, 2022] applies the Tensor Decomposition on 3D grids, substantially reducing the model size but still remaining notably larger than implicit approaches. 3DGS [Kerbl *et al.*, 2023] represents a scene with collections of explicitly represented Gaussians, where millions of Gaussians are required for high-fidelity modeling, resulting in substantial model sizes.

Hybrid Scene Representation

Typical hybrid representations entail the explicit storage of implicit features, which are inferred into concrete spatial attributes dynamically using neural networks. DVGO [Sun *et al.*, 2022] stores spatial features within volumetric 3D grids, albeit with huge space complexity. InstantNGP [Müller *et al.*, 2022] enhances this by incorporating multi-resolution 1D hash-tables, allowing positions with identical hashing values to share features. Point-NeRF [Xu *et al.*, 2022] adopts discrete 3D points to store spatial features. In summary, hybrid representations generally amalgamate the flexible nature of implicit representation and the high time efficiency of explicit ones. Similarly, our Gaussian-Forest is constructed based on a hybrid representation of 3D Gaussian.

Ray Tracing-based Rendering

NeRF [Mildenhall *et al.*, 2020] trains and renders scenes via differentiable ray marching. Subsequent research has primarily adopted this rendering approach, where some endeavors have concentrated on enhancing rendering efficiency and geometry representation. InstantNGP [Müller *et al.*, 2022] maintains cascade occupancy grids to skip ray marching in empty space. Mip-NeRF360 [Barron *et al.*, 2022] introduces a proposal network to provide a rapid and approximate scene estimation. VolSDF [Yariv *et al.*, 2021] and NeuS [Wang *et al.*, 2021] extend this rendering to represent signed distance function (SDF) fields, achieving high-quality surface reconstruction. However, the dense sampling nature of ray tracing poses challenges in meeting real-time rendering demands.

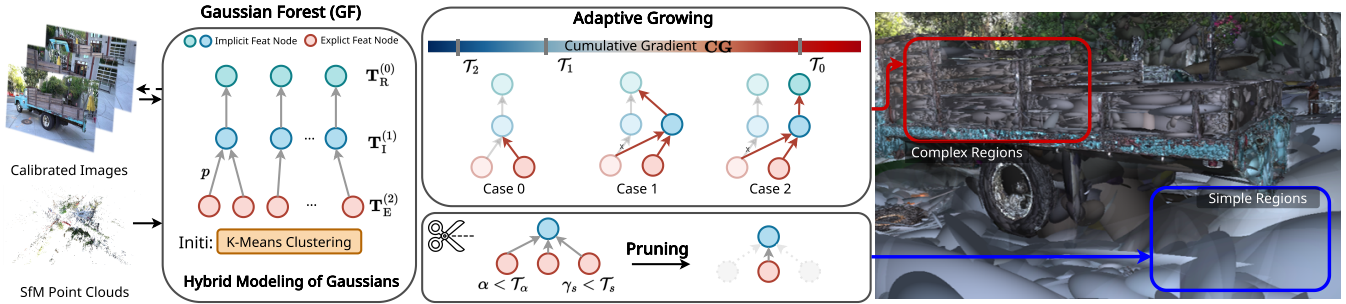


Figure 2: **Overview of the proposed Gaussian-Forest.** Gaussian-Forest hierarchically represents a scene as a forest composed of hybrid Gaussians, where non-leaf nodes capture their implicit attributes, while leaf nodes characterize explicit ones. Initiated from a compact set of singly linked lists, Gaussian-Forest adaptively grows in complex regions based on cumulative gradients to swiftly fit the scene. Leaf nodes with scaling and opacity below certain thresholds are considered trivial and subsequently removed. Such node count control ensures compact representations without compromising rendering quality while contributing to the acceleration of both training and rendering.

Rasterization-based Rendering

Recent advancements have propelled differentiable rasterization [Loper and Black, 2014; Li *et al.*, 2018; Yifan *et al.*, 2019] into the forefront. In [Kato *et al.*, 2018], an approximate gradient solution for differentiable silhouette rasterization is introduced. [Liu *et al.*, 2019] formulates view rendering as an aggregation function, paving the way for learning full attributes of mesh from color supervisions. Diverging from these polygon mesh-based approaches, Pulsar [Lassner and Zollhofer, 2021] proposes a fast differentiable rasterizer based on 3D spheres. Inspired by this innovation, 3DGS [Kerbl *et al.*, 2023] further improves by employing anisotropic 3D Gaussians instead of isotropic spheres and a rasterizer that respects visibility ordering. Rasterization’s fast rendering speed and ease of integration with modern hardware position it as a promising avenue for further research.

3 Method

3.1 Preliminaries and Task Formulation

3D Gaussian Splatting (3DGS) [Kerbl *et al.*, 2023] aims to model an arbitrary 3D scene with a set of anisotropic 3D Gaussians $\{\mathbf{G}_i\}_{i=1}^N$, which are initialized from structure-from-motion (SfM) sparse point clouds. Mathematically, each Gaussian is determined by the point mean position $\boldsymbol{\mu}$ and covariance matrix $\boldsymbol{\Sigma}$ in 3D space:

$$\mathbf{G}_i(\mathbf{x}) = e^{-\frac{1}{2}(\mathbf{x}-\boldsymbol{\mu})^\top \boldsymbol{\Sigma}^{-1}(\mathbf{x}-\boldsymbol{\mu})}, \quad (1)$$

where \mathbf{x} denotes an arbitrary point position. To ensure the covariance matrix is positive semi-definite throughout the optimization, it is formulated as $\boldsymbol{\Sigma} = \mathbf{R}\mathbf{S}\mathbf{S}^\top \mathbf{R}^\top$ with a rotation matrix \mathbf{R} and a scaling matrix \mathbf{S} . Specifically, each Gaussian is explicitly parameterized with a group of parameters Θ :

$$\Theta := \{\boldsymbol{\mu}, (\mathbf{q}, \mathbf{s}), \alpha, \mathbf{c}\} \in \mathbb{R}^{59}, \quad (2)$$

where $\mathbf{q} \in \mathbb{R}^4$, $\mathbf{s} \in \mathbb{R}^3$ are covariance-related quaternion and scaling vectors. $\alpha \in \mathbb{R}$ stands for the opacity for the subsequent blending process. To account for color variations with viewing angles, each Gaussian’s color is modeled by 4-order spherical harmonics (SH), represented as $\mathbf{c} \in \mathbb{R}^{3 \times 4^2}$. After training, the Gaussian parameters are determined, thus allowing the acquisition of the transformed 2D Gaussian on the

image plane. Subsequently, a tile-based rasterizer is applied to sort N Gaussians for α -blending. Typically, modeling a real-world scene may require several million Gaussians. This substantial quantity, along with the 59 parameters associated with each Gaussian, significantly increases the storage requirements for the trained model and affects rendering speed during the sorting and blending process.

To propose a more streamlined and practical solution, we propose Gaussian-Forest (GF), as illustrated in Fig. 2. Gaussian-Forest models Gaussian parameters within a hybrid tree, where each leaf node traces a distinct path to the root, thereby determining a specific Gaussian. Explicit attributes (e.g., position, opacity) are stored in the leaf nodes, while implicit attributes like scaling, rotation, and color are learned in the internal and root layers to maximize sharing across trees and reduce parameter redundancy (Sec. 3.2). Furthermore, to minimize the required number of Gaussians without compromising accuracy, the forests are dynamically grown and pruned (Sec. 3.3), focusing on adding siblings to accurately represent complex regions only.

3.2 Gaussian-Forest Modeling

The objective of building the Gaussian-Forest structure is to enable individual Gaussians to retain their unique *explicit* properties for capturing distinct local areas, while simultaneously sharing common *implicit* attributes across the scene to reduce the number of free parameters represented in Eq. (2). Towards this, we realize this structure through a tree composed of L layers, with L set to 3 without loss of generality. Higher levels of trees will contain fewer nodes with features of higher dimensions to maximize the benefits of sharing. Herein, we introduce the hybrid modeling of tree nodes.

Hybrid Tree Nodes. The architecture consists of three distinct node types: leaf node \mathbf{T}_E encapsulating explicit attributes, internal node \mathbf{T}_I , and root node \mathbf{T}_R , both dedicated to implicit attribute modeling. Each node type is characterized by a unique set of parameters:

$$\begin{aligned} \mathbf{T}_E^{(2)} &:= \{\boldsymbol{\mu}, \gamma_s, \alpha, p^{(2)}\} \in \mathbb{R}^6, \\ \mathbf{T}_I^{(1)} &:= \{\mathbf{f}_I, p^{(1)}\} \in \mathbb{R}^{D_I+1}, \mathbf{T}_R^{(0)} := \{\mathbf{f}_R\} \in \mathbb{R}^{D_R}, \end{aligned} \quad (3)$$

with the superscript indicating the node depth within the tree.

Among these notations, γ_s functions as the scaling coefficient for the implicit scaling \mathbf{s} , p represents an integer index pointer, and \mathbf{f} signifies a feature vector, with further elaboration following. The rationale beyond this hybrid modeling of Gaussian parameters lies in the fact that explicit attributes like position $\boldsymbol{\mu}$ and opacity α are agnostic to the viewing angle. Conversely, view-dependant attributes like covariance-related rotation \mathbf{q} , scaling \mathbf{s} , and colors \mathbf{c} are prone to redundancy. This motivates us to model them implicitly and designate significantly *fewer* nodes at higher levels, i.e., $N_R \ll N_I \ll N$, where N_R and N_I represents the number of root and internal nodes, respectively. All these number are adaptively adjusted during the forest’s growth and pruning processes (Sec. 3.3).

Leaf Node Traversal. Under the formulation of Eq. (3), the pointer $p^{(l)}$ stored at node $\mathbf{T}^{(l)}$ in the l -th layer establishes a link from $\mathbf{T}^{(l)}$ to its parent node at the $(l - 1)$ -th layer. By recursively tracing pointers upwards, each leaf node $\mathbf{T}_E^{(2)}$ traverses a unique path $[\mathbf{T}_E^{(2)}, \mathbf{T}_I^{(1)}, \mathbf{T}_R^{(0)}]$ leading to the root $\mathbf{T}_R^{(0)}$ of its corresponding tree, collectively defining the parameters of a distinct Gaussian. For the representation of implicit attributes, we concatenate the latent features along this path as $\mathbf{f} = [\mathbf{f}_I, \mathbf{f}_R] \in \mathbb{R}^{\mathcal{D}_I + \mathcal{D}_R}$.

View-dependent Implicit Attributes. To model the implicit attributes, we employ two MLP \mathcal{F}_{cov} and \mathcal{F}_{rgb} to decode the obtained latent features \mathbf{f} . This decoding results in: (1) the covariance-related scaling \mathbf{s} and rotation vectors \mathbf{q} , and (2) the view-dependent color \mathbf{c} , as shown below:

$$\mathbf{s} = \gamma_s \sigma(\hat{\mathbf{s}}), \hat{\mathbf{s}}, \mathbf{q} = \mathcal{F}_{\text{cov}}(\mathbf{f}), \quad (4)$$

where σ indicates a sigmoid activation. The color decoding process additionally incorporates the viewing direction $\vec{\mathbf{d}}$ of the camera as input:

$$\mathbf{c} = \mathcal{F}_{\text{rgb}}(\mathbf{f}, \vec{\mathbf{d}}). \quad (5)$$

This hierarchical representation offers efficiency advantages by reducing over 80% of parameters while retaining adaptability and expressive capabilities. Detailed theoretical and empirical analyses regarding storage size are presented in Sec. 4.4. In conclusion, Gaussian parameterization in Eq. (2) can be rewritten as:

$$\Theta_{\text{GF}} := \{\boldsymbol{\mu}, \mathcal{F}_{\text{cov}}(\mathbf{f}; \gamma_s), \alpha, \mathcal{F}_{\text{rgb}}(\mathbf{f}, \vec{\mathbf{d}})\}. \quad (6)$$

This formulation minimizes the number of parameters for each Gaussian component. However, this minimization is effective only when the total number of nodes is controlled. In the subsequent section, we elaborate on strategies for optimizing the Gaussian-Forest structure.

3.3 Forest Growing and Pruning

To control the number of nodes required for scene modeling, Gaussian-Forest is initialized as a small set of *singly linked lists* and undergoes adaptive growth and pruning to evolve into an efficient and robust forest. Specifically, branches exhibiting underfitting or high uncertainty are selectively expanded by adding more leaf and/or non-leaf nodes. In order to prevent excessive growth of the forest, we implement early stopping and pruning strategies. These approaches are pivotal in maintaining a concise yet faithful presentation, accelerating both the training and rendering processes.

Initialization

With the given SfM point cloud containing N_{SfM} points, we correspondingly establish N_{SfM} leaf nodes with explicit attributes initialized according to 3DGS [Kerbl *et al.*, 2023]. Following this, we initialize the root and internal layer, with each layer comprising K nodes where $K \ll N_{\text{SfM}}$. Nodes in two consecutive layers are interconnected in a one-to-one manner. Subsequently, we employ the K-means algorithm to group the leaf nodes into K clusters based on proximity. Each leaf node is then connected to an internal node corresponding to its cluster, thereby forming N_{SfM} singly linked lists. All implicit feature vectors in $\mathbf{T}_I^{(1)}$ and $\mathbf{T}_R^{(0)}$ are randomly initialized. For scenes like Synthetic Blending [Mildenhall *et al.*, 2020] with no available SfM point clouds, leaf nodes are initialized using $N_{\text{SfM}} = 100\text{k}$ synthetic points generated by uniform sampling following 3DGS [Kerbl *et al.*, 2023].

Forest Growth

To adapt to varying complexities in different scenes, a hierarchical forest growth strategy is leveraged based on cumulative gradients CG of leaf nodes during the end-to-end optimization. These gradients serve as indicators of the learning difficulty for each of the N Gaussians. Specifically, we consider three distinct cases governed by a set of gradient thresholds denoted by $\{\mathcal{T}_l\}_{l \in [0, L]}$ arranged in non-increasing order, while nodes beyond these three cases remain unchanged.

Case 0: $\mathcal{T}_2 < \text{CG} \leq \mathcal{T}_1$. For leaf nodes satisfying this case, growth is limited to their own cloning, creating a new link to each of their original parent nodes. This aligns with the split strategy in 3DGS [Kerbl *et al.*, 2023].

Case 1: $\mathcal{T}_1 < \text{CG} \leq \mathcal{T}_0$. For leaf nodes satisfying this case, both leaf and their parent internal nodes are cloned, with the original leaf node and its clone redirected toward the newly formed internal node.

Case 2: $\text{CG} \geq \mathcal{T}_0$. For leaf nodes satisfying this case, a complete cloning of all nodes along the paths to their roots is executed, resulting in the formation of a new linked list for each of them.

All these cases are illustrated in Figure 2. The motivation behind this hierarchical design is that a minimal cumulative gradient of a Gaussian implies the sufficient representational capacity for its local area. Hence, simpler background regions can be effectively modeled with fewer Gaussians. Conversely, a high cumulative gradient indicates the need for more detailed features, especially in complex regions like object boundaries or areas varying from different angles. To address this, both the leaves and their parent nodes are replicated, and the original leaves and their clones are then linked to the newly formed non-leaf nodes, thereby enhancing the model’s ability to depict these intricate areas with finer detail through increased feature dimensions.

Early Stopping

To avoid excessive expansion, we restrict forest growth to early stages, gradually stopping the expansion of higher-level nodes and limiting growth to leaf nodes in the final phase. Subsequently, all growth ends, and we concentrate on pruning. This process is regulated by predetermined stopping points t_l for each layer, ensuring efficient and targeted development during training.

Table 1: Quantitative comparisons on Mip-NeRF360, Tanks&Temples, Deep Blending and Synthetic Blender datasets. The best and second-best outcomes are shown in bold deep blue and light blue, respectively. All scores for compared methods are sourced from published papers or released pre-trained models, except for the hyphen (-) indicating no valid data and \dagger signifying re-evaluation on our machine.

Method	Mip-NeRF360						Tanks&Temples					
	FPS	MB	FPS/MB	SSIM \uparrow	PSNR \uparrow	Train	FPS	MB	FPS/MB	SSIM \uparrow	PSNR \uparrow	Train
Plenoxels [Fridovich-Keil <i>et al.</i> , 2022]	6.79	2150	0.003	0.626	23.08	26 m	13.0	2355	0.006	0.719	21.08	25 m
NGP-Base [Müller <i>et al.</i> , 2022]	11.7	13	0.900	0.671	25.30	6 m	17.1	13	1.315	0.723	21.72	5 m
NGP-Big [Müller <i>et al.</i> , 2022]	9.43	48	0.196	0.699	25.59	8 m	14.4	48	0.300	0.745	21.92	7 m
Mip-360 [Barron <i>et al.</i> , 2022]	0.06	8.6	0.007	0.792	27.69	48 h	0.14	8.6	0.016	0.759	22.22	48 h
3DGS [Kerbl <i>et al.</i> , 2023]	134	734	0.183	0.815	27.21	42 m	154	411	0.375	0.841	23.14	27 m
3DGS \dagger [Kerbl <i>et al.</i> , 2023]	105	827	0.127	0.816	27.45	28 m	143	454	0.315	0.848	23.73	16 m
GaussianForest-Large	105	85	1.235	0.803	27.45	28 m	164	45	3.644	0.839	23.67	16 m
GaussianForest-Small	121	50	2.426	0.797	27.33	26 m	175	38	4.605	0.836	23.56	15 m

Method	Deep Blending						Synthetic Blender					
	FPS	MB	FPS/MB	SSIM \uparrow	PSNR \uparrow	Train	FPS	MB	FPS/MB	SSIM \uparrow	PSNR \uparrow	Train
Plenoxels [Fridovich-Keil <i>et al.</i> , 2022]	11.2	2765	0.004	0.795	23.06	28 m	-	778	-	0.958	31.71	11 m
NGP-Base [Müller <i>et al.</i> , 2022]	3.26	13	0.251	0.797	23.62	7 m	-	13	-	0.963	33.18	5 m
NGP-Big [Müller <i>et al.</i> , 2022]	2.79	48	0.058	0.817	24.96	8 m	-	-	-	-	-	-
Mip-360 [Barron <i>et al.</i> , 2022]	0.09	8.6	0.010	0.901	29.40	48 h	-	8.6	-	0.961	33.09	48 h
3DGS [Kerbl <i>et al.</i> , 2023]	137	676	0.203	0.903	29.41	36 m	-	-	-	-	33.32	-
3DGS \dagger [Kerbl <i>et al.</i> , 2023]	106	701	0.151	0.904	29.54	25 m	344	72	4.778	0.969	33.80	7 m
GaussianForest-Large	96	98	0.980	0.908	30.18	29 m	417	11	37.91	0.969	33.60	7 m
GaussianForest-Small	107	64	1.672	0.905	30.11	25 m	445	8.5	52.71	0.967	33.52	6 m

Forest Pruning

Forest growth plays a crucial role in enhancing the model’s ability to represent complex regions. Nevertheless, this expansion may lead to an excessive increase in the number of both leaf and non-leaf nodes, consequently giving rise to redundant Gaussians. In response to this challenge, we develop a pruning strategy focused on eliminating redundant and non-essential Gaussians. As illustrated in Fig. 2, this strategy involves evaluating the explicit attributes of each leaf node, i.e., scaling vector \mathbf{s} and opacity α . If these attributes fall below predefined thresholds, denoted as \mathcal{T}_s for scaling and \mathcal{T}_α for opacity, the corresponding leaf nodes are deemed trivial and are thus removed to free up memory. The reasoning behind such pruning stems from the observation that Gaussians with minimal contributions to the α -blending process, as suggested by their low scaling and opacity values, exert a negligible impact on the model’s overall representational quality. Additional inspections are conducted after each pruning to identify and eliminate nodes with no children.

4 Experiments

4.1 Implementation Details

Framework and Hardware. Our Gaussian-Forest is implemented based on 3DGS [Kerbl *et al.*, 2023] and PyTorch. All experiments were conducted on a GeForce RTX 3090 GPU, which shares the same CUDA compute capability (8.6) as the RTX A6000 GPU used in 3DGS [Kerbl *et al.*, 2023]. For fair comparison, we re-executed their code on our machine.

Forest Structure. We instantiate the Gaussian-Forest as a composition of trees with $L = 3$ layers: one root layer, one internal layer, and one leaf layer. Each implicit layer is initialized with $K = 10\text{k}$ nodes, and the feature dimensions

for each layer are specified as $\{\mathcal{D}_R, \mathcal{D}_I\} = \{24, 16\}$ and $\{32, 24\}$ for the Large and Small settings, respectively.

Forest Growth. Forest growth occurs every 100 iterations, with growth thresholds set at $\{\mathcal{T}_I\} = \{1 \times 10^{-3}, 2.5 \times 10^{-4}, 2 \times 10^{-4}\}$. The number of iterations to stop the growth of each layer is defined as $\{t_i\} = \{5\text{k}, 10\text{k}, 15\text{k}\}$, and the training process concludes after the 30k iterations.

Forest Pruning. Gaussians with $\alpha < \mathcal{T}_\alpha$ or $\gamma_s < \mathcal{T}_s$ are identified and pruned every 100 iterations, where $\{\mathcal{T}_\alpha, \mathcal{T}_s\} = \{1 \times 10^{-2}, 5 \times 10^{-4}\}$. In contrast to the early-stop strategy for forest growth, pruning continues until the end of training, with a larger interval defined as 1,000 iterations.

Features and Decoders. The two MLPs, \mathcal{F}_{rgb} and \mathcal{F}_{cov} , are implemented using the fast fully-fused-MLPs from Tiny-CUDA-NN. Each MLP consists of 2 hidden layers and is 64 neurons wide. All features are represented in 16-bit half-float, aligning with the output of the fully-fused-MLPs.

4.2 Comparative Methods

3DGS [Kerbl *et al.*, 2023] stands out for its SOTA performance in rendering speed and quality, albeit with a substantial model parameter count. We primarily compare our approach with 3DGS, as we aim to preserve or even enhance the rendering speed and quality while reducing the parameter count. Additionally, we compared with three advanced ray tracing-based radiance field methods: Plenoxels [Fridovich-Keil *et al.*, 2022], based on explicit scene representation; Instant-NGP [Müller *et al.*, 2022], utilizing a hybrid representation; and Mip-NeRF360 [Barron *et al.*, 2022], employing implicit representation. These three approaches represent typical examples of different scene representation methods. Contrasting with them allows for a comprehensive demonstration of the characteristics of our method.

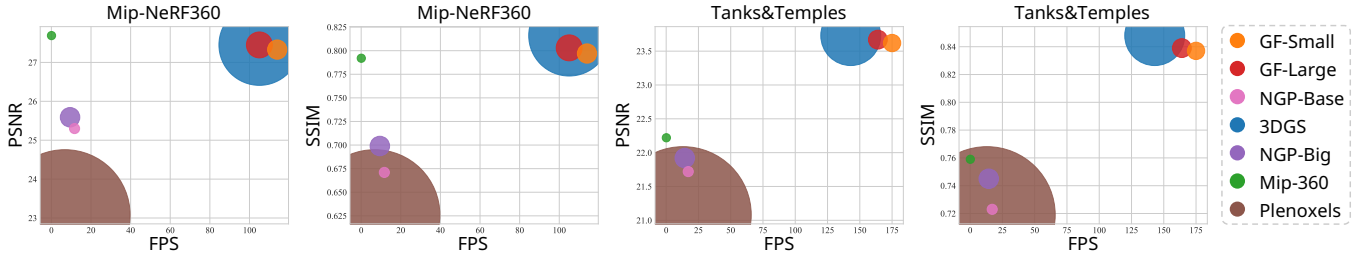


Figure 3: Visualization of quantitative comparisons on Mip-NeRF360 and Tanks & Temples datasets. The horizontal and vertical axes represent rendering speed and quality, respectively. Each point’s size in the figure indicates the corresponding model size in MB.

4.3 Datasets and Metrics

Following 3DGS, our model has been evaluated across 21 diverse scenarios. Of these, 13 scenes are based on real-world captures, including all nine scenes introduced by Mip-NeRF360 [Barron *et al.*, 2022], two scenes from the Tanks&Temples dataset [Knapitsch *et al.*, 2017], and two from Deep Blending [Hedman *et al.*, 2018]. Additionally, all eight synthetic scenes from the Synthetic Blender dataset [Mildenhall *et al.*, 2020] are incorporated. These datasets encompass large-scale unbounded outdoor environments, indoor settings, and object-centric scenes. We employ commonly used PSNR, SSIM [Wang *et al.*, 2004], and LPIPS [Zhang *et al.*, 2018] for evaluating rendering quality. Moreover, we provide information on rendering speed, model size, and training time, along with the speed-to-size ratio for a comprehensive and straightforward comparison.

4.4 Results and Analyses

Quantitative Comparisons

Quantitative results across four benchmarks are presented in Table 1, accompanied by additional visualizations for quantitative comparisons on Mip-NeRF360 and Tanks&Temples showcased in Fig. 3. Firstly, our approach excels in adeptly balancing rendering speed and model size. Across all scenarios, Gaussian-Forest achieves the highest speed-to-size ratio, surpassing all other comparative methods by a large margin while ensuring high-fidelity rendering quality.

In addition, compared to the unprecedentedly fast real-time rendering speed achieved by 3DGS, our method not only maintains comparable rendering quality across all test scenarios but also achieves further improvements in rendering speed and training speed. This enhancement is attributed to the substantial reduction in the number of Gaussians facilitated by our adaptive growth and pruning strategies. Most notably, coupled with the efficient scene representation and Gaussian management of Gaussian-Forest, our method achieves a remarkable 7 ~ 17 times reduction in model size compared to 3DGS, depending on the dataset and settings. Beyond the advantages of faster rendering speed and a significantly reduced model size, our approach has remarkably exceeded the rendering quality achieved by 3DGS on Deep Blending. This thoroughly validates the effectiveness of our approach.

Qualitative Comparisons

In Fig. 4, we present a comprehensive comparison of rendering quality between our Gaussian-Forest and 3DGS [Kerbl *et al.*, 2023], as well as representative ray tracing-based methods, including Mip-NeRF360 [Barron *et al.*, 2022] and In-

stantNGP [Müller *et al.*, 2022]. Across four scenes from distinct datasets, our findings reveal comparable or even superior quality in the synthesis of novel views. This achievement is coupled with the fastest rendering speed, as well as a remarkable compression of parameters exceeding ten-fold and notable improvements in both training and rendering speeds compared with the current state-of-the-art 3DGS. These outcomes substantiate the efficacy of our proposed method, aligning perfectly with quantitative results.

Complexity Analysis

Assuming 3DGS necessitates N Gaussians for scene modeling, its spatial complexity stands at $O(59N)$. In Gaussian-Forest, explicit attributes of each hybrid Gaussian are represented by 6 parameters in its corresponding leaf node, yielding a spatial complexity of $O(6N)$. Post-adaptive growth, the root and internal nodes account for about 1.5% ~ 2.5% and 25% ~ 50% of leaf nodes, respectively. Under the configuration of $\{\mathcal{D}_R, \mathcal{D}_I\} = \{24, 16\}$ and 16-bit half-float feature format, the spatial complexity of non-leaf nodes ranges from $O(2.2N)$ to $O(4.3N)$ (excluding negligible parameters for MLPs and integer pointers in internal nodes). Furthermore, our pruning strategy effectively reduces leaf nodes by 1.5 ~ 3 times and non-leaf nodes by about 1.5 times. In the end, the overall space complexity ranges from $O(3.5N)$ to $O(7N)$, yielding a compression factor of approximately 8 ~ 17, aligning seamlessly with the quantitative results. Such a reduction in Gaussian count has also accelerated both training and rendering speed, completely offsetting the time complexity introduced by the inclusion of MLPs.

4.5 Ablation Study

We conducted ablation studies on Deep Blending (DB) scenes [Hedman *et al.*, 2018] to validate the Gaussian-Forest components: hybrid Gaussian representation, forest management, adaptive growth, and pruning strategy. Hyperparameter impact was also investigated, including growth and pruning thresholds, and feature dimensions of non-leaf nodes. The following baselines were set:

+Hybrid: Employment of hybrid Gaussian defined in Eq. (6), with a trivial feature association by storing features in a hash table [Müller *et al.*, 2022] for coordinate-based lookups. We adjusted the table size T to control the model’s capabilities with $T = \{18, 19, 20, 21, 22, 23\}$.

+Forest: Management of hybrid Gaussians in a forest as defined in Eq. (3), with non-growing root and internal nodes. To investigate the impact of feature dimensions, we conducted



Figure 4: Qualitative comparisons illustrating rendering quality, with images generated from held-out test views.

three sets of experiments, labeled *A*, *B*, and *C*, with $\{\mathcal{D}_R, \mathcal{D}_I\} = \{16, 8\}$, $\{24, 16\}$, and $\{32, 24\}$, respectively.

+Growth: Management of hybrid Gaussians in a forest as defined in Eq. (3), with adaptive growth of non-leaf nodes. To quantitatively illustrate the impacts of growth thresholds $\{\mathcal{T}_l\}$, we delineated four configurations, labeled *A*, *B*, *C*, and *D*, with $\{\mathcal{T}_l\} = \{10, 5, 2\}$, $\{10, 2.5, 2\}$, $\{5, 5, 2\}$, and $\{5, 2.5, 2\}$, respectively (in 10^{-4} units).

+Pruning: Management of hybrid Gaussians in a forest as defined in Eq. (3), with both adaptive growth and pruning of non-leaf nodes, forming our comprehensive Gaussian-Forest model. To investigate the impact of the scale pruning threshold \mathcal{T}_s , we define seven settings, labeled *A*, *B*, *C*, *D*, *E*, *F*, and *G*, with $\mathcal{T}_s = \{1, 10, 100, 300, 500, 700, 900\}$, respectively (in 10^{-6} units).

The results in Fig. 5 show that using hybrid Gaussians significantly reduces space requirements. However, trivial feature association negatively affects scene representation capability and rendering quality. Managing hybrid Gaussians within a static forest structure has limited superiority due to constraints imposed by relying on initialized feature nodes. Incorporating adaptive growth enables the Gaussian forest to rapidly model complex areas, enhancing scene modeling and rendering quality while keeping a compact model size. Adaptive pruning identifies and eliminates redundant Gaussians, further reducing parameters without compromising rendering accuracy. In conclusion, these findings underscore the effectiveness of our proposed Gaussian-Forest.

5 Conclusion

In this paper, we present a solid solution to the storage issues associated with 3DGS in the context of compressed scene modeling. The introduced Gaussian-Forest, with its

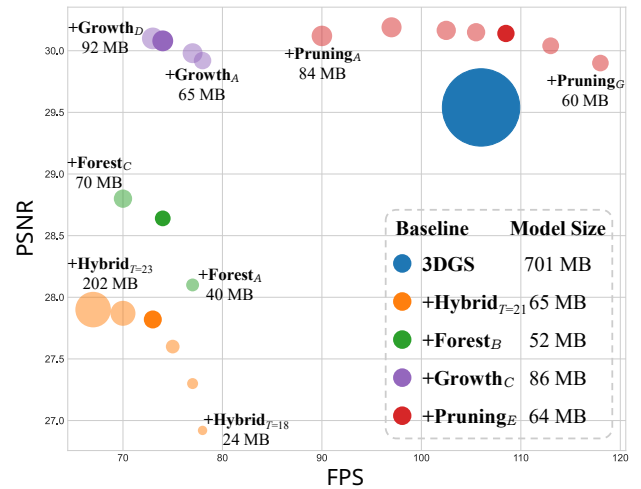


Figure 5: Ablation experimental results on Deep Blending scenes. The size of each point in the figure correlates with the respective model size in MB, and each baseline is distinguished by a unique color, with their optimal configurations highlighted in the darkest shade. Furthermore, the legend displays the model sizes corresponding to these optimal settings. To ensure clarity and intuitiveness, only the initial and final points are annotated in the figure for the other parameter settings of each baseline.

hierarchical hybrid representation, effectively organizes 3D Gaussians into a forest structure, optimizing parameterization and addressing storage constraints. The incorporation of adaptive growth and pruning strategies ensures detailed scene representation in intricate areas while substantially reducing the overall number of Gaussians. Through extensive experiments, we demonstrate that Gaussian-Forest maintains rendering speed and quality comparable to 3DGS, while achieving an impressive compression rate exceeding 10 times.

References

- [Barron *et al.*, 2022] Jonathan T. Barron, Ben Mildenhall, Dor Verbin, Pratul P. Srinivasan, and Peter Hedman. Mip-NeRF 360: Unbounded anti-aliased neural radiance fields. In *IEEE/CVF Computer Vision and Pattern Recognition Conference*, pages 5460–5469, 2022.
- [Cao and Johnson, 2023] Ang Cao and Justin Johnson. Hex-Plane: A fast representation for dynamic scenes. In *IEEE/CVF Computer Vision and Pattern Recognition Conference*, pages 130–141, 2023.
- [Chen *et al.*, 2022] Anpei Chen, Zexiang Xu, Andreas Geiger, Jingyi Yu, and Hao Su. TensorRF: Tensorial radiance fields. In *European Conference on Computer Vision*, pages 333–350, 2022.
- [Deng *et al.*, 2022] Kangle Deng, Andrew Liu, Jun-Yan Zhu, and Deva Ramanan. Depth-Supervised NeRF: Fewer views and faster training for free. In *IEEE/CVF Computer Vision and Pattern Recognition Conference*, pages 12882–12891, 2022.
- [Fridovich-Keil *et al.*, 2022] Sara Fridovich-Keil, Alex Yu, Matthew Tancik, Qinhong Chen, Benjamin Recht, and Angjoo Kanazawa. Plenoxels: Radiance fields without neural networks. In *IEEE/CVF Computer Vision and Pattern Recognition Conference*, pages 5501–5510, 2022.
- [Hedman *et al.*, 2018] Peter Hedman, Julien Philip, True Price, Jan-Michael Frahm, George Drettakis, and Gabriel Brostow. Deep blending for free-viewpoint image-based rendering. *ACM Transactions on Graphics*, 37(6):257:1–15, 2018.
- [Kato *et al.*, 2018] Hiroharu Kato, Yoshitaka Ushiku, and Tatsuya Harada. Neural 3D mesh renderer. In *IEEE/CVF Computer Vision and Pattern Recognition Conference*, pages 3907–3916, 2018.
- [Kerbl *et al.*, 2023] Bernhard Kerbl, Georgios Kopanas, Thomas Leimkühler, and George Drettakis. 3D Gaussian splatting for real-time radiance field rendering. *ACM Transactions on Graphics*, 42(4):139:1–14, 2023.
- [Kim *et al.*, 2022] Mijeong Kim, Seonguk Seo, and Bohyung Han. InfoNeRF: Ray entropy minimization for few-shot neural volume rendering. In *IEEE/CVF Computer Vision and Pattern Recognition Conference*, pages 12912–12921, 2022.
- [Knapitsch *et al.*, 2017] Arno Knapitsch, Jaesik Park, Qian-Yi Zhou, and Vladlen Koltun. Tanks and Temples: Benchmarking large-scale scene reconstruction. *ACM Transactions on Graphics*, 36(4):78:1–13, 2017.
- [Lassner and Zollhofer, 2021] Christoph Lassner and Michael Zollhofer. Pulsar: Efficient sphere-based neural rendering. In *IEEE/CVF Computer Vision and Pattern Recognition Conference*, pages 1440–1449, 2021.
- [Li *et al.*, 2018] Tzu-Mao Li, Miiika Aittala, Frédo Durand, and Jaakko Lehtinen. Differentiable monte carlo ray tracing through edge sampling. *ACM Transactions on Graphics*, 37(6), 2018.
- [Liu *et al.*, 2019] Shichen Liu, Tianye Li, Weikai Chen, and Hao Li. Soft rasterizer: A differentiable renderer for image-based 3d reasoning. In *IEEE/CVF International Conference on Computer Vision*, pages 7707–7716, 2019.
- [Liu *et al.*, 2020] Lingjie Liu, Jiatao Gu, Kyaw Zaw Lin, Tat-Seng Chua, and Christian Theobalt. Neural sparse voxel fields. In *Conference on Neural Information Processing Systems*, volume 33, pages 15651–15663. Curran Associates, Inc., 2020.
- [Loper and Black, 2014] Matthew M. Loper and Michael J. Black. OpenDR: An approximate differentiable renderer. In *European Conference on Computer Vision*, pages 154–169, 2014.
- [Mildenhall *et al.*, 2020] Ben Mildenhall, Pratul P. Srinivasan, Matthew Tancik, Jonathan T. Barron, Ravi Ramamoorthi, and Ren Ng. NeRF: Representing scenes as neural radiance fields for view synthesis. In *European Conference on Computer Vision*, pages 405–421, 2020.
- [Müller *et al.*, 2022] Thomas Müller, Alex Evans, Christoph Schied, and Alexander Keller. Instant neural graphics primitives with a multiresolution hash encoding. *ACM Transactions on Graphics*, 41(4):102:1–15, 2022.
- [Niemeyer *et al.*, 2022] Michael Niemeyer, Jonathan T. Barron, Ben Mildenhall, Mehdi S. M. Sajjadi, Andreas Geiger, and Noha Radwan. RegNeRF: Regularizing neural radiance fields for view synthesis from sparse inputs. In *IEEE/CVF Computer Vision and Pattern Recognition Conference*, pages 5480–5490, 2022.
- [Pumarola *et al.*, 2021] Albert Pumarola, Enric Corona, Gerard Pons-Moll, and Francesc Moreno-Noguer. D-NeRF: Neural radiance fields for dynamic scenes. In *IEEE/CVF Computer Vision and Pattern Recognition Conference*, pages 10318–10327, 2021.
- [Sun *et al.*, 2022] Cheng Sun, Min Sun, and Hwann-Tzong Chen. Direct voxel grid optimization: Super-fast convergence for radiance fields reconstruction. In *IEEE/CVF Computer Vision and Pattern Recognition Conference*, pages 5449–5459, 2022.
- [Wang *et al.*, 2004] Z. Wang, A. Bovik, H. Sheikh, and E. Simoncelli. Image quality assessment: From error visibility to structural similarity. *IEEE Transactions on Image Processing*, 13(4):600–612, 2004.
- [Wang *et al.*, 2021] Peng Wang, Lingjie Liu, Yuan Liu, Christian Theobalt, Taku Komura, and Wenping Wang. NeuS: Learning neural implicit surfaces by volume rendering for multi-view reconstruction. In *Conference on Neural Information Processing Systems*, pages 27171–27183, 2021.
- [Wei *et al.*, 2021] Yi Wei, Shaohui Liu, Yongming Rao, Wang Zhao, Jiwen Lu, and Jie Zhou. NerfingMVS: Guided optimization of neural radiance fields for indoor multi-view stereo. In *IEEE/CVF International Conference on Computer Vision*, pages 5610–5619, 2021.
- [Xu *et al.*, 2022] Qiangeng Xu, Zexiang Xu, Julien Philip, Sai Bi, Zhixin Shu, Kalyan Sunkavalli, and Ulrich Neumann. Point-NeRF: Point-based neural radiance fields. In

- IEEE/CVF Computer Vision and Pattern Recognition Conference*, pages 5428–5438, 2022.
- [Yariv *et al.*, 2021] Lior Yariv, Jiatao Gu, Yoni Kasten, and Yaron Lipman. Volume rendering of neural implicit surfaces. In *Conference on Neural Information Processing Systems*, pages 4805–4815, 2021.
- [Yifan *et al.*, 2019] Wang Yifan, Felice Serena, Shihao Wu, Cengiz Öztireli, and Olga Sorkine-Hornung. Differentiable surface splatting for point-based geometry processing. *ACM Transactions on Graphics*, 38(6), 2019.
- [Yu *et al.*, 2022] Zehao Yu, Songyou Peng, Michael Niemeyer, Torsten Sattler, and Andreas Geiger. MonoSDF: Exploring monocular geometric cues for neural implicit surface reconstruction. In *Conference on Neural Information Processing Systems*, volume 35, pages 25018–25032, 2022.
- [Yuan *et al.*, 2022] Yu-Jie Yuan, Yang-Tian Sun, Yu-Kun Lai, Yuewen Ma, Rongfei Jia, and Lin Gao. NeRF-Editing: Geometry editing of neural radiance fields. In *IEEE/CVF Computer Vision and Pattern Recognition Conference*, pages 18353–18364, 2022.
- [Zhang *et al.*, 2018] Richard Zhang, Phillip Isola, Alexei A. Efros, Eli Shechtman, and Oliver Wang. The unreasonable effectiveness of deep features as a perceptual metric. In *IEEE/CVF Computer Vision and Pattern Recognition Conference*, pages 586–595, 2018.
- [Zhou *et al.*, 2023] Xingchen Zhou, Ying He, F. Richard Yu, Jianqiang Li, and You Li. RePaint-NeRF: NeRF editing via semantic masks and diffusion models. In *International Joint Conferences on Artificial Intelligence*, pages 1813–1821, 2023.